Influence of Geometric Parameters on Overall Performance of High Bypass Ratio Turbofan Nacelle and Exhaust System

W. J. Wang, L. Zhou[†], Z. X. Wang, and J. W. Shi

Shaanxi key laboratory of internal aerodynamics in aero-engine, School of Power and Energy, Northwestern Polytechnical University, Xi'an, 710129, China

†*Corresponding Author Email*: *zhouli@nwpu.edu.cn*

ABSTRACT

In order to understand the coupled effect of the nacelle and exhaust system and to improve their overall performance, we studied the aerodynamic performance and the flow characteristics of the high bypass ratio turbofan nacelle and exhaust system by numerical simulation. The geometric parameters of a nacelle and exhaust system (e.g., the contraction ratio of the cowl afterbody and the fan nozzle exit angle) were investigated to evaluate their influence on the overall performance of the nacelle and exhaust system. The related flow mechanism was explored as well. The results show that the flow field of the nacelle and exhaust system under the mid-cruise condition exhibits characteristics of transonic flow. A stagnation zone exits at the nacelle lip and there is a velocity peak at the nacelle forebody. There exist a number of complex flow phenomena (such as shockwave, expansion wave, shear flow and shock wave-boundary layer interaction) in the downstream of the fan nozzle exit plane. The magnitude of the fan nozzle thrust or the intake ram drag is much higher than that of the additional drag, the nacelle drag or the core nozzle thrust. And for the nacelle drag, the friction drag of the cowl is in the same order of magnitude as the pressure drag of the cowl, the core cowl and the plug. But it is much larger than the friction drag of the core cowl and the plug. The effective thrust increases by 4.7% as the contraction ratio of the cowl afterbody increases; and it increases by 2.4% as the fan nozzle exit angle increases. The expansion degree of the fanjet flow, the shock wave strength and location, and the existence of the flow separation or second shock wave are influenced by the contraction ratio of the cowl afterbody and the fan nozzle exit angle. These phenomena have effects on the pressure distribution of the core cowl and the surrounding fanjet flow velocity, and hence they further affect the nacelle drag. The increase in the fan nozzle exit angle can noticeably reduce the thrust of the fan nozzle.

Keywords: Nacelle; Exhaust system; Coupled influence; Effective thrust.

NOMENCLAUTURE

A_{out}	exit area of nozzle	D	drag
A_{01}	area of engine capture stream tube	D_{Add}	additional drag
A_1	highlight area	$D_{CoreCowl}$	core cowl drag
A	super ellipse semi major axis	D_{Cowl}	cowl drag
B	super ellipse semi minor axis	D_R	ram drag
C_d	drag coefficient	$FNEA$	fan nozzle exit angle
$C_{d,Add}$	additional drag coefficient	$FNPR$	fan nozzle pressure ratio
$C_{d,CoreCowl}$	core cowl drag coefficient	Ma_{ise}	isentropic Mach number
$C_{d,Cowl}$	cowl drag coefficient	$MFCR_d$	mass flow capture ratio at design point
$C_{d,Plug}$	plug drag coefficient	T_{CN}	core nozzle gross thrust
$C_{d,f}$	friction drag coefficient	T_{Eff}	effective thrust of engine
$C_{d,p}$	pressure drag coefficient	T_{FN}	fan nozzle gross thrust
$CNEA$	core nozzle exit angle	T_{t13}	total temperature at the inlet of fan nozzle
$CNPR$	core nozzle pressure ratio	T_{t5}	total temperature at the inlet of core
C_p	pressure coefficient		

	nozzle	p_t	total pressure
u	velocity component in X direction	p_{te}	total pressure at the border line of boundary layer
u_0	free stream velocity in X direction		
$\vec{V}$	velocity vector	p_0	free stream pressure
$\vec{V}_0$	free stream velocity vector	ρ	density
		ρ_0	free stream density
W	mass flow rate of engine	τ	$[\vec{\tau}_x\ \vec{\tau}_y\ \vec{\tau}_z]$matrix of viscous stresses
$\vec{n}$	outward unit normal vector		
n_x	components of $\vec{n}$ in X-direction	$\vec{\tau}_x$	$[\tau_{xx}\ \tau_{xy}\ \tau_{xz}]$vector of viscous stresses
p	static pressure		

1. INTRODUCTION

New engine concepts and technologies for civil aircraft, such as distributed propulsion (Gohardani *et al.* 2011; Isikveren *et al.* 2015), boundary layer ingestion (Singh *et al.* 2014; Blumenthal *et al.* 2012) and counter rotating open rotors (Schnell *et al.* 2012), were developed for a long-term goal to reduce operation costs, environmental impact and aerodynamic noises. At the same time, efforts were made to improve the performance of high bypass ratio (HBPR) turbofans owing to the rich technical accumulation and fairly good feasibility. The research on high bypass ratio turbofan mainly concentrates on two aspects. On the one hand, the improvement in the performance of components, such as compressor (Lin *et al.* 2019; Peyvan & Benisi 2016), combustor (Yangaz *et al.* 2016), and so on, is used to improve the thermal efficiency of the engine and on the other hand, the study on increasing the bypass ratio of civil turbofan engine is conducted at the same time. The advantage of the HBPR turbofan with low fan pressure ratio (FPR) lies in that the low exhaust velocity can lead to an improvement in the propulsion efficiency, a decrease in the specific fuel consumption (SFC), and a reduction in the jet engine noises. However, a problem which comes up with the HBPR turbofan is that the increasing fan diameter leads to a larger and heavier nacelle. And more importantly, the nacelle drag becomes higher and higher with the increase of the nacelle wetted area. Relevant studies (Hoheisel 1997) have shown that the contribution of a nacelle to a typical twin-engine aircraft drag is around 14%. A rise in BPR also results in higher ram drag because of the higher engine mass flow rate. It is necessary to compensate for the ram drag by increasing the gross force of the exhaust system. As a result, the effect of the exhaust system on the net engine thrust becomes more serious than ever before. In addition, there is obvious interaction between the nacelle and the exhaust system in terms of the geometry and the flow characteristic. Furthermore, the nacelle and the exhaust system need to be as short as possible to achieve a lighter design of modern ultra-high bypass ratio turbofans nacelle, and it makes their coupling effect even stronger. The surfaces of the nacelle and the exhaust system are simultaneously depending on some geometric parameters. Thus it is worth exploring the interaction between the nacelle and the exhaust system by studying the influence of these geometric parameters on their overall aerodynamic performance and flow characteristics.

In earlier investigations, researchers studied the nacelle (or the exhaust system) by replacing the other with an oversimplified model or by just leaving it alone due to the complexity of the problem. Joo *et al.* (2012) examined the influence of Mach number and the mass flow capture ratio (MFCR) on the nacelle drag and the related flow mechanism while they neglected the influence of the exhaust system by replacing the exhaust system with an extended section. Christie *et al.* (2017) studied the characteristics of the drag rise with the increasing Mach number, spillage drag with the decreasing engine mass flow rate and the distortion at fan face with increasing angle of attack by replacing the exhaust system with a cylindrical surface. Li and Zhong performed natural laminar nacelle optimization by simplifying the exhaust system as a cylindrical surface (Li and Zhong 2014; Zhong and Li 2017). Fang *et al.* (2016) conducted a nacelle optimization design based on the design of experiments (DOE), numerical simulation, response surface model and hybrid genetic algorithm. However, the length, the trailing edge diameter and the boattail angle of the nacelle were treated as constraints rather than design variables in their study.

Robinson *et al.* (2017) carried out performance optimization for the nacelle with three different values in the length-diameter ratio based on DOE, numerical simulation, surrogate model, and non-dominated sorting genetic algorithm (NSGA-II). Their study showed that compared to longer nacelles, the design space is much narrower and there are significant penalties in the off-design conditions for the short nacelle. Xiong *et al.* (2012) performed optimization design for a separate-exhaust system based on parallel multi-objective genetic algorithm and numerical simulation. In this study, the length, the exit diameter and the fan nozzle exit angle were set as the design variables in order to achieve the maximum thrust and the shortest length of the exhaust system. They achieved an increase in the total thrust of the exhaust system by around 0.5% or a reduction in the total length by 2%. Goulos *et al.* optimized the performance of a separate-exhaust system by considering the influence of the nacelle (Goulos *et al.* 2016a; b). They achieved an increase in the total thrust of the exhaust system by 0.4 - 3.4% after optimizing the design of the duct and the nozzle. The design of the core cowl and zone 3 vent
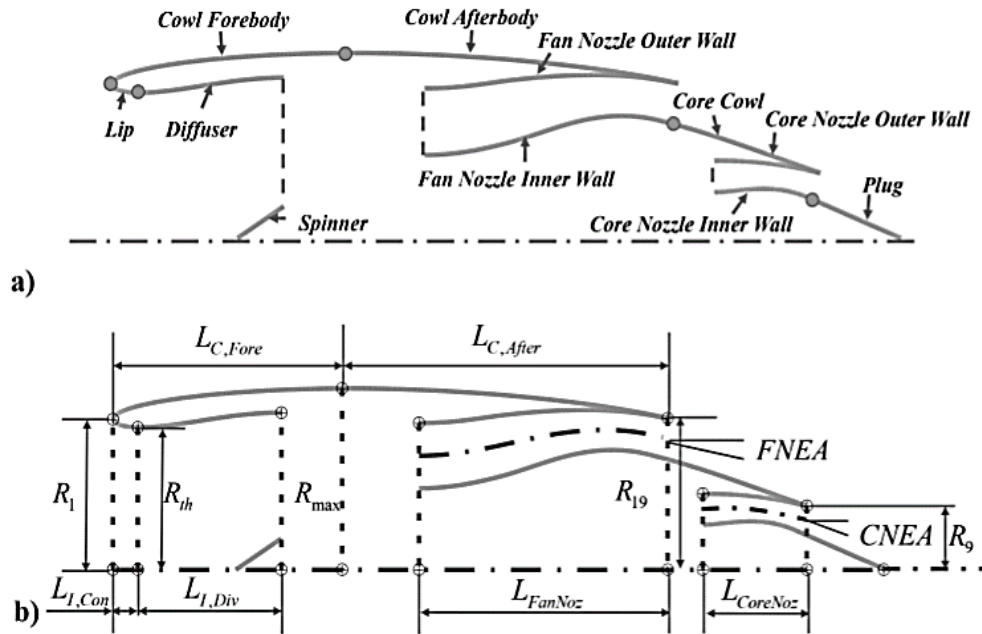
Fig. 1. Nacelle and exhaust system: a) the geometry and b) the key parameters.

exhaust nozzle were optimized such that the length of the core cowl was decreased by 15%. Savelyev *et al.* (2014) optimized the aerodynamic performance of the nacelle and the exhaust system separately via numerical simulation and coordinate descent method. As a result, the effective thrust was raised by 1.2%; the maximum Mach number around the surface of the cowl was reduced from 1.22 to 1.08 and the overall length of the nacelle and exhaust system was shortened by 300 mm.

There are a few reports in the literature regarding the coupled influence and the integrated design of the nacelle and exhaust system. Qiang (2013) developed the design method and carried out integration for the nacelle and exhaust system. Wang *et al.* (2019) investigated the influence of the length- diameter ratio of the fan nozzle on the overall performance and flow characteristics of the nacelle and exhaust system. They found that the effective thrust increases by 3.2% as a result of the decrease in the length-diameter ratio of the fan nozzle, and that the pressure drag on the core cowl is the dominant factor affecting the nacelle drag and the effective thrust for various fan nozzle length-diameter ratios.

In this work, an integrated model was established for the HBPR turbofan nacelle and exhaust system. A numerical simulation method was first developed and validated. Then the flow characteristics of the nacelle and exhaust system were studied through numerical simulation. We examined the influence of the geometric parameters (e.g., the contraction ratio of the cowl afterbody and the fan nozzle exit angle) on the overall aerodynamic performance of the nacelle and exhaust system, and we further explored the related flow mechanism.

2. GEOMETRIC MODEL AND NUMERICAL SIMULATION METHOD

2.1 Geometric Model

In this section, we established a turbofan engine model with the bypass ratio equaling to 10. The integrated model of the nacelle and exhaust system was designed based on the flight parameters, the thermodynamic parameters and the structural dimension parameters of the engine model acquired by engine cycle analysis and size estimation under the mid-cruise condition.

Figure 1a illustrates the geometric model of the nacelle and exhaust system. The nacelle/exhaust system model consists of the intake, the cowl, the fan nozzle inner/outer wall, the core nozzle inner/outer wall, the core cowl and the plug. Figure 1b shows the definition of the key parameters for the nacelle and exhaust system. The intake is described by the parameters including the highlight radius R_1, the radius of the intake throat R_{th}, the lip length $L_{I, Con}$ and the length of the intake diffuser section $L_{I, Div}$; the cowl is described with the parameters including the highlight radius R_1, the forebody length of the cowl $L_{C, Fore}$, the maximum radius of the cowl R_{max}, the afterbody length of the cowl $L_{C,After}$, the trailing edge radius of the cowl $R_{C, Te}$ and the cowl boattail angle *CBA*. And the exhaust system is described using the parameters: the fan nozzle length L_{FanNoz}, the exit radius of the fan nozzle R_{19}, the fan nozzle exit angle FNEA, the core nozzle length $L_{CoreNoz}$, the exit radius of the core nozzle R_9 and the core nozzle exit angle *CNEA*.

Table 1 Values of key geometric parameters of nacelle and exhaust system baseline model

Parameters	Values	Parameters	Values
$MFCR_d$	0.75	$D_{max}/D19$	1.21
R_1/R_{th}	1.055	$L_{FanNoz}/D13,O$	0.84
$L_{I,Con}/L_{Intake}$	0.127	$L_{CoreNoz}/D5,O$	0.64
$L_{Intake}/D2$	0.5	$D9,O/D19,O$	0.42
$L_{C,Fore}/L_{Nac}$	0.42	$FNEA$	$13.5°$
$D_{A,max}/D1$	1.17	$CNEA$	$21°$
$L_{Nac}/D1$	1.69	/	/

The intake consists of a lip and a diffuser. The intake lip is described by a super ellipse equation, as

$$(x \, / \, a)^m + (y \, / \, b)^n = 1 \tag{1}$$

where a and b denote the semi-major axis and the semi-minor axis of the super ellipse, respectively ($a = L_{I,Con}$ and $b = R_1 - R_{th}$). The diffuser section is created via cubic polynomial curve. The cowl is subdivided into two regions: the fore-body and the afterbody, which are described by a quadratic curve. The quadratic curve is defined by

$$a_{11}x^2 + 2a_{12}xy + a_{22}y^2 + 2a_{13}x + 2a_{23}y + a_{33} = 1 \tag{2}$$

where $a_{11}^2 + a_{12}^2 + a_{22}^2 \neq 0$. The exhaust system consists of four parts, namely the fan nozzle, the core nozzle, the core cowl and the plug. The design of the exhaust system can be simplified as profile design as its geometry is axisymmetric. The nozzle is modeled by a centerline and the area distribution. The cubic spline interpolation is employed to define the centerline and Lee curves (Lee and Boedicker 1985) are utilized to define the area distribution. The core cowl is designed with a cubic polynomial curve and the plug with a line. The slope of two adjacent curves should be equal at the connection points.

The geometric constraints put forward by Hei (2016) are given as follows:

1. The trailing edge diameter of the cowl is equal to the exit diameter of the fan nozzles outer wall;

2. The length of the fan nozzle is equal to the length of the nacelle subtracting the length of the intake and the length of the fan casing;

3. The cowl boattail angle is equal to the fan nozzle exit angle.

Based on these geometric constraints between the nacelle and the exhaust system, $L_{C,After}$, $R_{C,Te}$, and CBA can be replaced with L_{FanNoz}, R_{19} and $FNEA$, respectively. It can be seen that the values of the fan nozzle length, the fan nozzle exit diameter and the fan nozzle exit angle can influence the profile of the cowl and the exhaust system, simultaneously. This means that these geometric parameters have an impact on the overall aerodynamic performance and the flow characteristic of the nacelle and exhaust system. The effect of the variation on the fan nozzle length is not considered in this paper as it has been discussed by Wang *et al.* (2019). The contraction ratio of the cowl afterbody is equal to the ratio of the maximum nacelle diameter to the trailing edge diameter of the cowl, and the fan nozzle exit angle is defined by the angle between the engine axis and the tangent line of the fan nozzles mid-surface side line at the endpoint. The normalized key design parameters are listed in Table 1.

2.2 Numerical Simulation Method

The commercial flow solver, FLUENT, is selected for the numerical simulation. The axisymmetric steady Reynolds-averaged N-S equations in the conservative form are numerically solved. Gao *et al.* (2019) conducted a numerical simulation on a transport airplane, including the high bypass ratio turbofan nacelle, where the $k - \varepsilon$ turbulence model was selected. Results show that the maximum errors of engine thrust and mass flow rate between the numerical simulation and experimental data are below 2% under different operation conditions. Thus, the $RNG\ k - \varepsilon$ turbulence model with scalable wall function was chosen as turbulence model in this paper. The convection terms and the viscous terms of the equations are discretized by second-order upwind scheme and second-order center scheme, respectively. The implicit density-based algorithm is used to solve the equations. The air is modeled as compressible ideal gas.

The computational domain and the boundary conditions are shown in Fig. 2. The computational domain is a rectangular region. The length of the rectangle is 160 times the maximum diameter of the nacelle. The width is 80 times the maximum diameter of the nacelle. The inlet and side of the domain are modeled as pressure far-field boundary condition, for which the static pressure, static temperature, Mach number and flow direction are prescribed. The outlet of the domain is applied with the pressure outlet condition, for which a uniformly distributed static pressure is specified. At the location of the fan face, the pressure outlet condition is prescribed with specified targeted mass flow rate. The inlets of the fan nozzle and the core nozzle are applied with pressure inlet conditions with uniform distribution of total pressure and total temperature. An impermeable, no-slipped and adiabatic wall boundary condition is applied to the wall of the nacelle and exhaust system. The boundary conditions of the fan face and the nozzle inlet were obtained by engine cycle analysis under mid-cruise
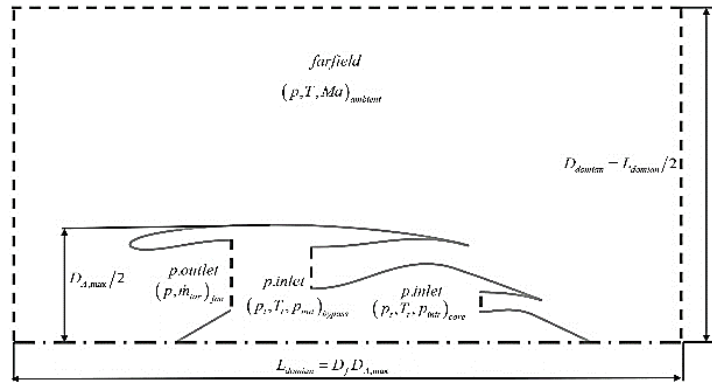
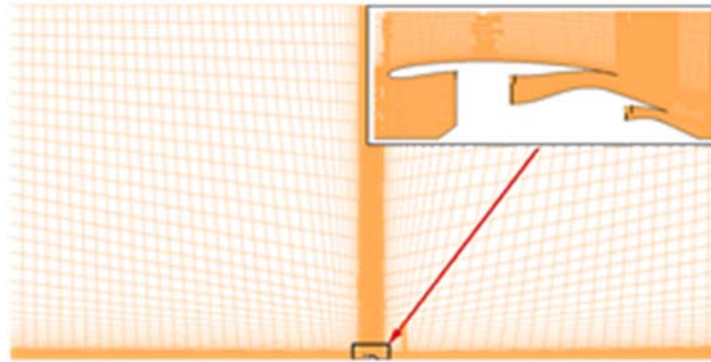**Fig. 2. CFD domain and boundary conditions setting.**

Fig. 3. Grids of nacelle and exhaust system.

condition. The boundary and flight conditions under the mid-cruise condition are listed in Table 2.

Table 2 Flight and boundary conditions

Parameters	Values	Parameters	Values
Ma	0.8	T_{t3}, *K*	285
MFCR	0.75	*CNPR*	1.81
H,m	10668	T_{t5}, *K*	722
FNPR	2.43	/	/

The multi-block structured mesh for the nacelle and exhaust system was generated by the commercial software ICEM. All wall-adjacent cells were refined by boundary layer grids. The maximum y^+ value of the first cells is around one to meet the requirements of the turbulence model. The grids around the nacelle and exhaust system are shown in Fig. 3.

2.3 Performance Parameters

Not only the performance of the nacelle but also the performance of the exhaust system is affected by the geometric parameters, such as the contraction ratio of the cowl afterbody and the fan nozzle exit angle. So the effective thrust is selected for the evaluation of the overall performance of the nacelle and exhaust system. The schematic of the force accounting for the computation of the thrust and drag is shown in Fig. 4.

The effective thrust is calculated, as

$$T_{Eff} = T_{FN} + T_{CN} - D_R - D_{Add} - D_{Nac} \quad (3)$$

The nozzle thrust and the ram drag of the intake is defined as follow:

$$T_N = \iint_{A_{out}} \rho u \vec{V} \bullet \vec{n} + (p - p_0)n_x dA \quad (4)$$

$$D_R = W u_0 \quad (5)$$

The definition of the additional drag is given by

$$D_{Add} = \iint_{A_{01}} (p - p_0)n_x dA \quad (6)$$

The nacelle drag is calculated by

$$D_{Nac} = D_{Cowl} + D_{CoreCowl} + D_{Plug} \quad (7)$$

The drag of the cowl, the core cowl or the plug is the sum of the pressure drag and the friction drag on its surface. The pressure drag and the friction drag are respectively defined by

$$D_p = \iint (p - p_0)n_x dA \quad (8)$$

$$D_f = \iint \vec{\tau}_x \bullet \vec{n} dA \quad (9)$$

In order to compare the amplitude of various components of the nacelle drag, the non-

dimensional drag coefficient C_d is defined, as

$$C_d = \frac{D}{\frac{1}{2}\rho_0 V_0^2 A_1}$$ (10)

where D is the drag of nacelle or its components, $\frac{1}{2}\rho_0 V_0^2$ is the dynamic pressure of free stream and A_1 is the highlight area of the nacelle. In this paper, we selected the values of the effective thrust and the nacelle drag coefficient of the baseline model as a reference, and then calculated the increment of the two quantities.

3. RESULTS AND DISCUSSIONS

3.1 Validation of Numerical Simulation Method and Grid Independence

In order to validate the reliability of the numerical simulation approach, we studied the flow field of the turbine powered simulator (TPS) nacelle and exhaust system model (Hirose *et al*. 1991) via numerical simulation. The experiment was performed in NAL $2m \times 2m$ Transonic Wind Tunnel in Japan National Aerospace Laboratory. The pressure distributions on the cowl and the core cowl surface were measured at zero incidence, Mach number 0 to 0.8 and turbine revolution from windmill to maximum speed. The numerically simulated test case was set at $Ma_\infty = 0.8$, $MFCR = 0.5234$, $FNPR = 1.43$, $FNTR = 1.133$, $CNPR = 1.125$, $CNPR = 1.125$. The computed pressure distribution on the cowl and the core cowl surface was compared with the experimental data, which were shown in Fig. 5. It can be seen that their comparison is fairly good. And it can be concluded that the numerical simulation method and the boundary conditions used in this paper are suitable to acquire the performance and the flow characteristics of the nacelle and exhaust system.
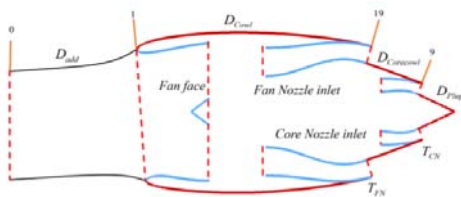

Fig. 4. Schematic of force accounting for the computation of thrust and drag.

The topology and the boundary layer of the mesh were introduced in section 2.2. The mesh size (or referred to as the cell number) causes uncertainty of the numerical results, too. Three mesh sizes, Mesh 1 with 63824 cells, Mesh 2 with 116554 cells and Mesh 3 with 222401 cells, were respectively used in the numerical simulation to evaluate the influence of the mesh size. The dimensionless effective thrust is given in Table 3 and the pressure coefficients with separate mesh sizes are presented in Figs.6. The difference among the effective thrust based on the

three mesh sizes is less than one percent. The maximum local error of the dimensionless static pressure is less than 1.6% of the pressure amplitude on the nacelle. The numerical results based on Mesh 2 and Mesh 3 are closer to each other. It can be concluded that the uncertainty induced by mesh size can be neglected when Mesh 2 is selected for numerical simulation.
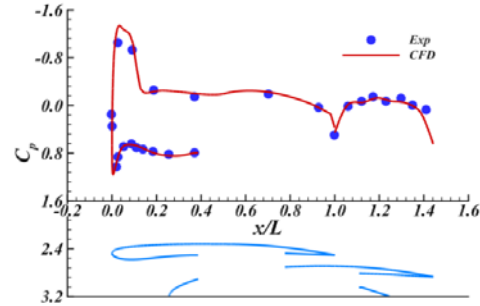

Fig. 5. Comparison of CFD results and experimental data.

Table 3 Dimensionless effective thrust with different cells number

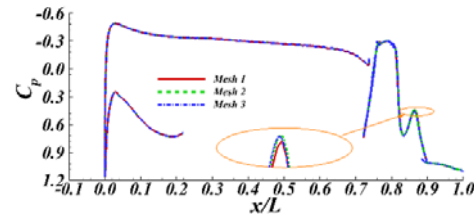| Cells number	63824	116554	222401
$T_{Eff}/T_{Eff,R}$	0.9989	1	1.0002

Fig. 6. Pressure coefficients comparison of cowl, core cowl and plug with different mesh size.

3.2 Aerodynamic Performance and Flow Characteristics

The difference between the air mass flowing out of the intake and the air mass flowing in the nozzle is below 0.01% of the engine mass flow rate. This means the mass flow rate error does not affect the quantities of the thrust and the drag acquired by the numerical simulation. The decomposition of the thrust and the drag of the nacelle and exhaust system is presented in Fig. 7. Although this decomposition cannot provide direct information to improve the overall performance of the nacelle and exhaust system, it could give rise to intuitive knowledge of the relative state of the thrust and the drag. Fig. 7 shows that the fan nozzle thrust and the ram drag of the intake are much higher than the additional drag, the nacelle drag, and the core nozzle thrust. The ram drag of the intake is mainly dependent on the flight velocity and the engine mass flow rate. The additional drag of the intake is mainly dependent on the flight conditions and the mass flow capture ratio. The axial gross thrust of the nozzle mainly depends on its inlet conditions, such as the total pressure, the

total temperature, the mass flow rate, and the geometric contour. The nacelle drag is not only affected by the profiles of the cowl, the core cowl, and the plug but also is related to the flight conditions and the given engine throttle condition. Moreover, three parts, namely the cowl, the core cowl, and the plug, are included in the nacelle drag components. The nacelle drag is further decomposed. It can be seen from Fig. 7 that the pressure drags of the cowl, the core cowl and the plug are in the same order of magnitude. The friction drag of the cowl, which is in the same order of magnitude as the above-mentioned pressure drag, is much higher than the friction drag of the core cowl or the plug.
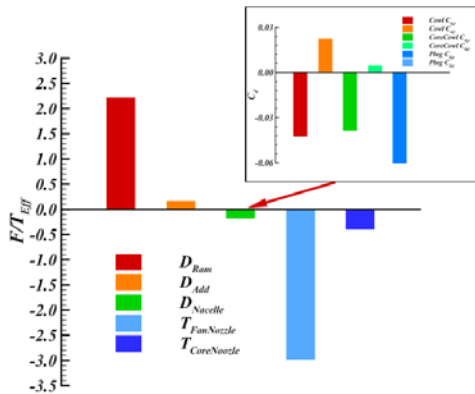
Fig. 7. Thrust/drag decomposition of nacelle and exhaust system.

The distribution of the pressure coefficient of the cowl is shown in Fig. 8. The isentropic Mach number, the boundary layer thickness, and the skin friction coefficient are presented in Figs. 9a, 9b, and 9c, respectively. It needs to be pointed out beforehand that one needs to find a way to acquire the isentropic Mach number distribution and the boundary layer thickness distribution. The simplification can be done when isentropic Mach number distribution and boundary layer thickness distribution were calculated because the aim is to analyze the skin friction coefficients distribution qualitatively. So the following assumptions were introduced.

1. The viscous effect out of boundary layer can be neglected;

2. The integration of the pressure gradient from the wall to the borderline of the boundary layer along the outside normal direction of the wall can be neglected; and

3. The total pressure at the borderline of the boundary layer is constant.

The curvature around the nacelle lip is large and the related pressure gradient in the boundary layer is large, too. Fortunately, the boundary layer is thin as it just appears there. The isentropic Mach number and the total pressure at the borderline of the boundary layer can be calculated, as

$$Ma_{ise} = \sqrt{\frac{2}{\gamma-1}[(\frac{p_t}{p_w})^{\frac{\gamma-1}{\gamma}}-1]} \qquad (11)$$

$$p_{te} = p_w [1+\frac{\gamma-1}{2}(0.99Ma_{sie})^2]^{\frac{\gamma}{\gamma-1}} \qquad (12)$$
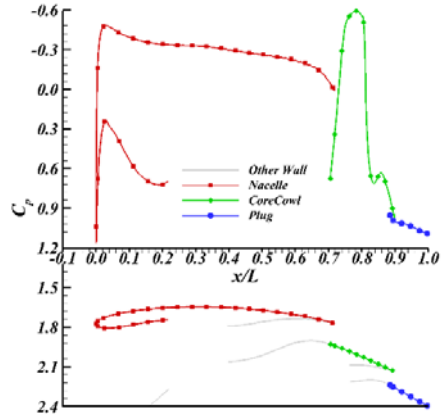
Fig. 8. Pressure coefficients distribution on the cowl, core cowl and plug.

The total pressure stays constant outside the boundary layer according to assumption 1. The static pressure at the borderline of the boundary layer can be replaced with the pressure on the wall based on assumption 2. Considering the total pressure loss resulted from the shock wave, we compared in Fig. 9a the isentropic Mach number calculated based on the total pressure in the upstream and downstream of the shock wave. The difference is so small that the influence of the total pressure loss resulting from the shock wave can be neglected in terms of the isentropic Mach number. According to assumption 3, in the total pressure contour of the nacelle and exhaust system, the borderline of the boundary layer can be acquired by the total pressure isoline. The total pressure for this isoline is equal to the mean value of the total pressure in the borderline of the boundary layer calculated via Eq. (12).

The Mach number contour of the nacelle and exhaust system is shown in Fig. 10. It can be seen that the flow field of the nacelle and exhaust system under the mid-cruise condition is of the characteristics of the typical transonic flow. Both the subsonic and supersonic zones exist around the nacelle and exhaust system. It can be seen from Fig. 10 that a low velocity and high-pressure zone appears at the lip of the nacelle due to the flow stagnation. Under the influence of the stagnation zone at the lip of the nacelle and the influence of the curvature distribution of the cowl forebody, the external flow around the cowl first accelerates and then decelerates. There exists a velocity peak on the forebody of the nacelle. The patterns of shock waves and expansion waves are seen in the fanjet stream around the core cowl as the fan nozzle is choked. The shock wave-boundary layer interaction exists on the core cowl, leading to a rapid increase in the boundary layer thickness. Moreover, it would cause boundary layer separation.

There are three streams in the flow field with different velocity, pressure, and temperature. In Fig. 10, one can notice the external shear layer between the free stream and the fanjet stream and the internal shear layer between the fanjet stream and the corejet stream.
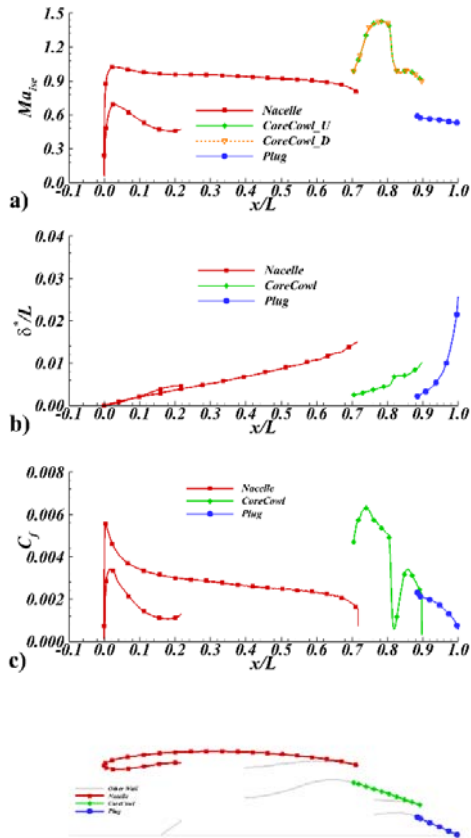
Fig. 9. Distribution of a) the isentropic Mach number, b) the boundary layer thickness, and c) the skin friction coefficient, on the surface of the cowl, the core cowl and the plug.

It can be seen that the skin friction coefficient increases rapidly due to the rapid increase in the flow velocity around the cowl forebody. And then the skin friction coefficient decreases because of the rapid increase in the boundary layer thickness while the flow velocity reduces slowly. There is a wall shear stress peak on the cowl forebody, but it is not at the same position as the velocity peak in the flow direction due to the influence of the thickening boundary layer along with the cowl. On the up-stream part of the core cowl, although the boundary layer thickness increase slowly, the skin friction coefficient increases rapidly due to the increase in the flow velocity, which is attributed to the rapid expansion of the fanjet flow downstream of the fan nozzle exit plane. While the fanjet flow passes through the shock wave that originated from the core cowl, the velocity decreases and the boundary layer thickens sharply. As a result, the skin friction coefficient reduces rapidly. The skin friction coefficient of the core cowl downstream of the first

shock wave reduces slowly. The main reason is that the flow velocity decreases and the boundary layer thickens slowly. The friction coefficient decreases monotonically on the plug as the corejet stream velocity reduces and the thickness of the boundary layer increases.

3.3 Influence of Contraction Ratio of Nacelle Afterbody

In this section, five axisymmetric nacelle and exhaust system models with different contraction ratios of the cowl afterbody are numerically simulated. The other design parameters of the models are the same as the baseline model. Comparisons of these models are presented in Fig. 11. It can be seen that the degree of shrinkage of the cowl afterbody increases and the curvature of the cowl decreases with the increasing contraction ratio of cowl afterbody. The crook degree of the fan nozzle becomes much smaller. Thus the curvature of the inner wall and the outer wall of the fan nozzle decrease. The degree of shrinkage of core cowl and the curvature of the core cowl both decrease.

The effective thrust with varied contraction ratios of the cowl afterbody is shown in Fig. 12. It can be seen that the effective thrust increases by 4.7%, with the increase in the contraction ratio of the cowl afterbody. The effective thrust is equal to the nozzle thrust minus the sum of the ram drag, the additional drag and the nacelle drag according to Eq. (3). In order to analyze the influence of the nozzle thrust and the influence of each drag above on the effective thrust, relative variations in selected types of force with varied contraction ratios of the cowl afterbody are shown in Fig. 13. It is noticed that the nacelle drag is the dominant factor affecting the effective thrust. The nacelle drag reduces with increasing contraction ratios of the cowl afterbody. The variation amplitude is about 4.8% of the effective thrust based on the baseline model. In order to examine the main factors that affect the nacelle drag, the relative variations in the pressure drag coefficient and the friction drag coefficient of the cowl, the core cowl, and the plug are provided in Fig. 14 with various contraction ratio of the cowl afterbody. It is found that the change in the pressure drag on the core cowl is the dominant factor affecting the nacelle drag. The pressure drag coefficient and the friction drag coefficient of the cowl decreases slightly with the increment in the contraction ratio of the cowl afterbody. The pressure drag coefficient of the core cowl decreases continuously. The variation trend of the friction drag coefficient of the core cowl is opposite to that of the pressure drag. The pressure drag and the friction drag of the plug increase slightly.

The influence of the contraction ratio of the cowl afterbody on the flow characteristic of the nacelle and exhaust system and the flow mechanism are discussed in the following. Figures 15a and 15b show the distribution of the pressure coefficient and the skin friction coefficient on the cowl, respectively. It is noticed in Fig. 15a that, as the contraction ratio of the cowl afterbody constantly increases, the static pressure on the surface of the cowl afterbody is raised and the velocity around the cowl afterbody is reduced
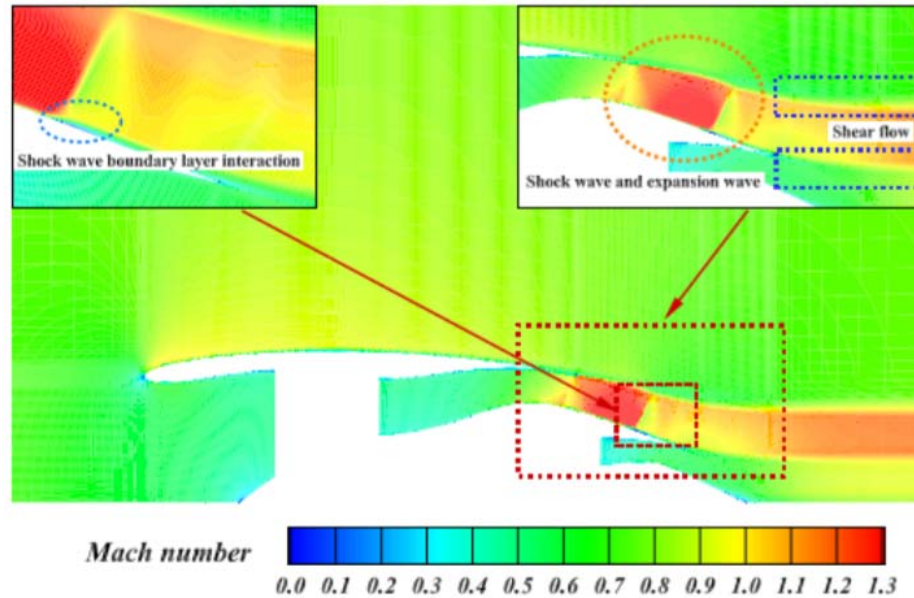
Fig. 10. Mach number contour of nacelle and exhaust system.

due to the increasing shrinkage degree and the decreasing curvature of the cowl afterbody. As a result, this leads to a decreasing wall shear on the cowl afterbody, as shown in Fig. 15b. At the same time, there is an increase in the projected area of the cowl afterbody, which is vertical to the engine axis. The increasing forward pressure force on the cowl afterboy caused by an increasing projected area reduces the pressure drag of cowl. So the pressure drag and the friction drag of the cowl decrease along with the increase in the contraction ratio of the cowl afterbody.
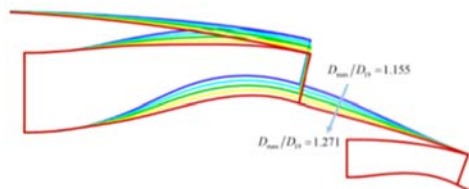
Fig. 11. Comparison of geometry with varied contraction ratios of cowl afterbody.

The comparison of the Mach number contour around the cowl afterbody and the exhaust system is shown in Fig. 16. It shows that the decrease in the convex degree of the core cowl leads to a decrease in the fanjet flow velocity. Mach number before the first shock wave reduces and the first shock wave becomes constantly weakened. The flow separation resulted from the first shock wave-boundary layer interaction shrinks and vanishes. It is further noticed that the first shock wave moves downstream and the supersonic zone enlarges. At the same time, the flow in the downstream of the first shock accelerates once more and the second shock wave appears and gets strengthened.

Figure 17a presents the comparison of static pressure on the core cowl and on the plug. It is found in Fig. 17a that there is a rapid increase in the static pressure on the core cowl for all the models and there is a smaller rapid increase in the static pressure around the terminal of the core cowl for the models with the contraction ratio of the cowl afterbody being 1.155 and 1.176. The rapid increase in the static pressure is caused by the shock wave. With the increase in the contraction ratio of the cowl afterbody, the static pressure on the core cowl upstream of the first shock wave increases. This means that the fanjet flow velocity decreases. The decrease in the convex degree of the core cowl is the main factor that leads to such a change in static pressure and fanjet velocity. At the same time, the static pressure downstream of the first shock wave decreases and the local velocity rises. This is attributed to the weakening of the first shock wave and the strengthening of the second acceleration of the local flow. It is further found that the high velocity and low pressure zone enlarges with the increment of the contraction ratio of the cowl afterbody as the first shock wave moves downstream. Figure 17b shows the comparison of the skin friction coefficient on the core cowl. It can be seen that being mainly affected by the fanjet velocity, the skin friction coefficient in upstream of the first shock wave increases and that in downstream of the first shock wave decreases with the increasing contraction ratio of cowl afterbody. There is one peak and two valleys for the skin friction coefficients after the first shock wave in the model with the contraction ratio being 1.155. This is mainly caused by the flow separation resulting from first shock wave boundary layer interaction. It can be found out that the projected area of core cowl, which is vertical to the engine axis reduces with the increases of contraction ratio of nacelle afterbody. The reducing projected area of core cowl would lead

to decreases in forward pressure force of core cowl, in other words, increases in pressure drag of core cowl. The drag of the core cowl is influenced by several factors, such as the Mach number before the first shock wave, the location, and strength of the first shock wave and the projected area of core cowl vertical to the engine axis. The effects of these factors are contradictory. The trend of the core cowl drag, which varies with the increase of the contraction ratio of the cowl afterbody, depends on the combined effect of these factors.
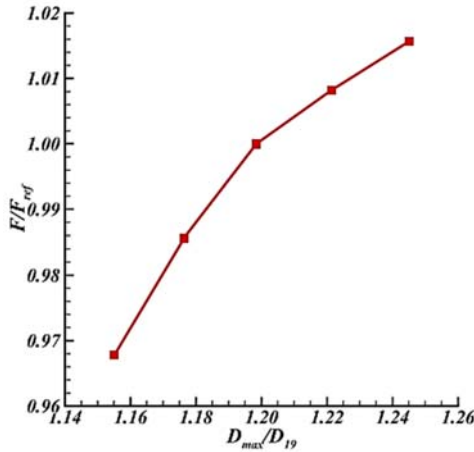
Fig. 12. Effective thrust with varied contraction ratios of the cowl afterbody.
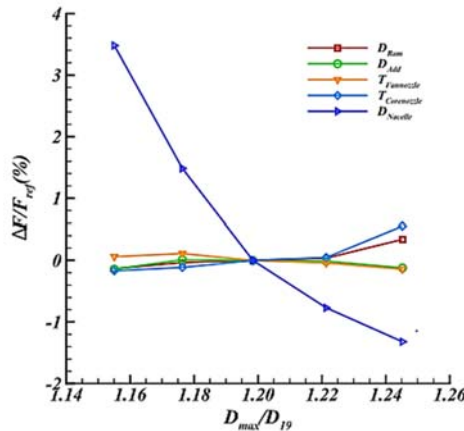
Fig. 13. Nacelle drag and the nozzle thrust with varied contraction ratios of the cowl afterbody.

It can be seen from Fig. 17a that the static pressure at exit plane of core nozzle decreases with the increase of contraction ratio of cowl afterbody. The reason for this is that the strengthening of the second acceleration of the local flow around core cowl. So, as shown in Figs. 17a and 17b, the static pressure on the plug decreases and the corejet flow velocity increases slightly with the contraction ratio of the cowl afterbody as the corejet flow expands more completely. The skin friction coefficients increase due to the increasing flow velocity. Therefore, the

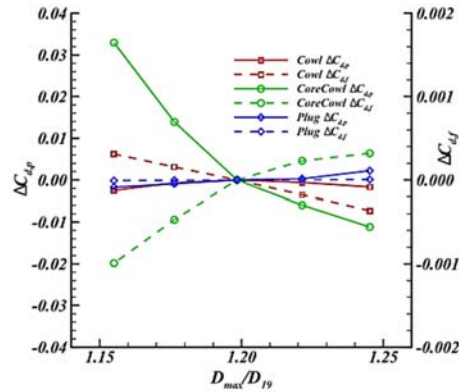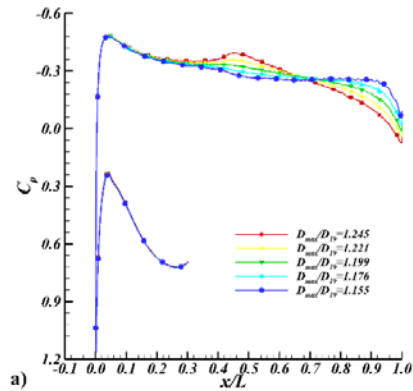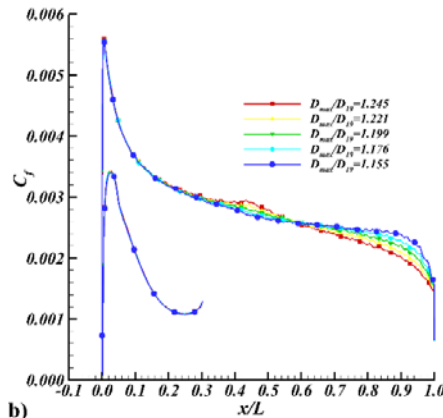pressure drag and the friction drag of the plug increase slightly with the contraction ratio of the cowl afterbody.

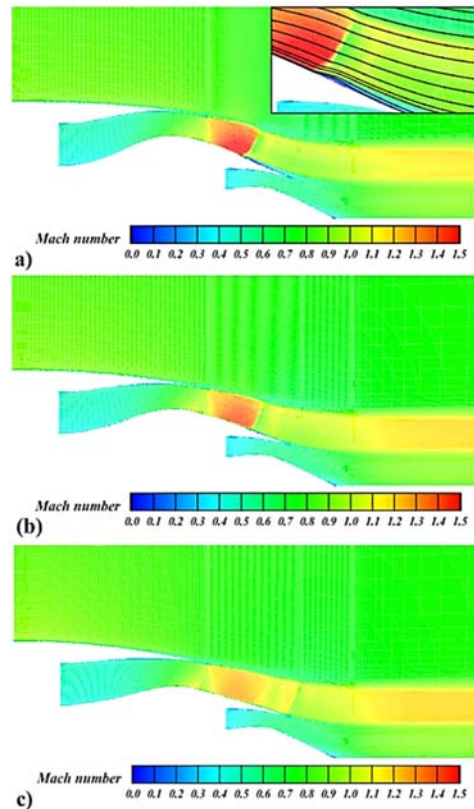**Fig. 14. Nacelle drag with varied contraction ratios of the cowl afterbody.**

Fig. 15. Comparison of the distribution of a) the pressure coefficients, and b) the skin friction co-efficients on the surface of the cowl.

Although the effective thrust is affected by several aspects, it is obvious that the nacelle drag is the dominating factor. So the variation trend of the effective thrust is opposite to that of the nacelle drag.

1968

Fig. 16. Comparison of Mach number contour with varied contraction ratios of cowl afterbody:

a) $\dfrac{D_{max}}{D_{19}} = 1.176$ **b)** $\dfrac{D_{max}}{D_{19}} = 1.221$ **c)**

$$\dfrac{D_{max}}{D_{19}} = 1.245$$

3.4 Influence of Fan Nozzle Exit Angle

Five models of the nacelle and exhaust system with various fan nozzle exit angle (10.5°, 12°, 13.5°, 15° and 16.5°) were numerically investigated. The other design parameters are the same as the baseline model. These five models are presented in Fig. 18. It can be seen that the curvature of the cowl increases due to the increase in the fan nozzle exit angle. The degree of the crook of the fan nozzle enhances, and it leads to a raised curvature of the inner and outer walls of the fan nozzle. On the contrary, as the fan nozzle exit angle keeps increasing, the value of the slope at the start point of the core cowl is getting closer to the value at the terminal point. This results in a decrease in the curvature of the core cowl.

The effective thrust with varied fan nozzle exit angles is shown in Fig. 19. It shows that the effective thrust increases by 2.4 % with the increasing fan nozzle exit angle. In Fig. 20, we plotted the ram drag, the additional drag, the nacelle drag and the nozzle thrust drag, which are varying with the fan nozzle exit angle. As shown in the figure, the nacelle drag and the fan nozzle

thrust are the main factors that affect the effective thrust. With the increase in the fan nozzle exit angle, the decrease in the nacelle drag and in the fan nozzle thrust is 9.2% and 6.7% of the amount of the effective thrust of the baseline model, respectively. The pressure drag and the friction drag of the cowl, the core cowl and the plug are shown in Fig. 21 with varied fan nozzle exit angle. It is noticed that the pressure drags of the cowl and the core cowl are the main factors that affect the nacelle drag. The pressure drag coefficient, the friction drag coefficient of the cowl and the friction drag coefficient of the core cowl all increase and the pressure drag coefficient of the core cowl decreases with the increment of the fan nozzle exit angle. The pressure drag coefficient and the friction drag coefficient of the plug are almost un-changed.
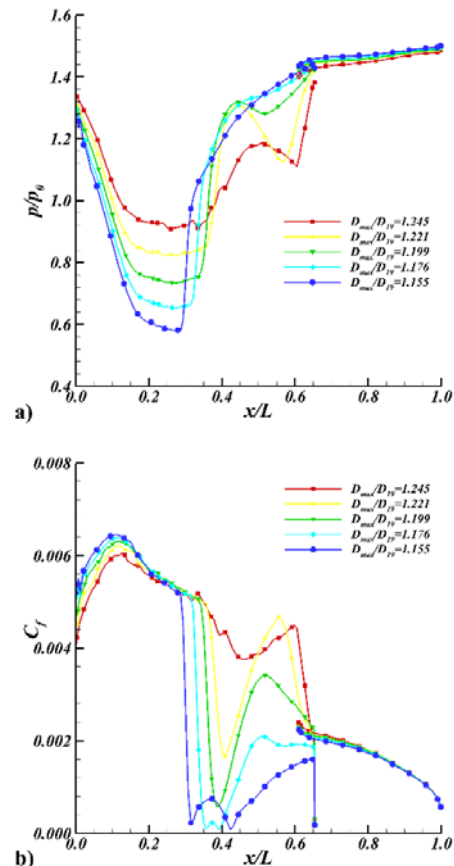
Fig. 17. Comparison of a) the dimensionless static pressure, and b) the skin friction coefficients distribution on the surface of the core cowl and the plug.

The fan nozzle thrust is the sum of the momentum force and the pressure force. The increase in the fan nozzle exit angle results in an increase in both the angle between the fanjet stream velocity and the engine axis and the angle between the pressure force and the engine axis. This leads to a decrease in the fan nozzle thrust. It can be seen in Fig. 22a that,

with the increase in the fan nozzle exit angle, there is an increase in the flow velocity around cowl afterbody and there is a decrease in the static pressure on the surface of the cowl afterbody. This is due to the increasing curvature of the cowl afterbody. The skin friction coefficient increases as a result of the increase in the flow velocity around the cowl afterbody, as shown in Fig. 22b. As such the pressure drag and the friction drag of the cowl increase.
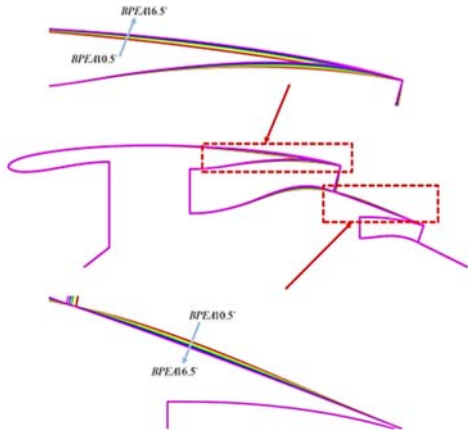

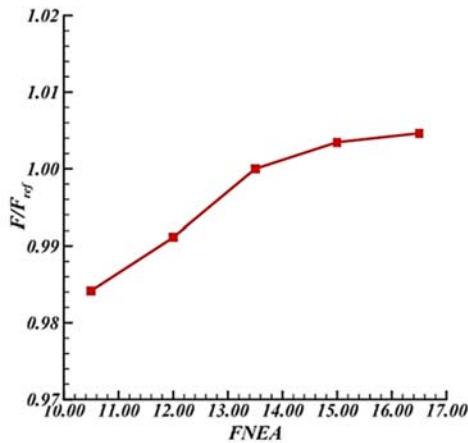**Fig. 18. Comparison of geometry with varied fan nozzle exit angle.**

Fig. 19. Effective thrust with varied fan nozzle exit angle.

The Mach number contours with varied fan nozzle exit angle are shown in Fig. 23. The fanjet flow velocity decreases due to the decreasing curvature of the core cowl. There is a decrease in the Mach number before the first shock wave that originated from the core cowl. As a result, the strength of the shock wave is weakened. The separation zone caused by the first shock wave-boundary layer interaction diminishes and disappears. The flow velocity in the downstream of the first shock wave increases and a second shock wave appears and gets strengthened.
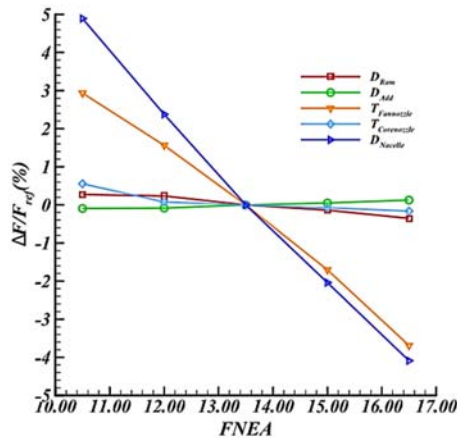

Fig. 20. Nacelle drag and nozzle thrust with varied fan nozzle exit angle.
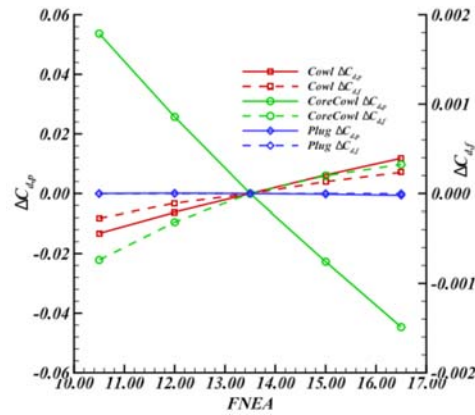

Fig. 21. Nacelle drag with varied fan nozzle exit angle.

Figure 24a shows the comparison of the distribution of the static pressure on the core cowl and the plug. There is a rapid increase in the static pressure on the core cowl for all the models, and there is a smaller rapid increase in the static pressure in the downstream of the first one for the models, wherein the fan nozzle exit angle is equal to 15° or 16.5°, respectively. As the fan nozzle exit angle increases, the static pressure in the upstream of the first shock wave increases and local fanjet flow velocity decreases. The main reason for this is that the curvature of the core cowl decreases as the fan nozzle exit angle increases. It is further found out that the static pressure on the core cowl in the downstream of the first shock wave decreases. The local fanjet flow velocity increases. There exists a valley of static pressure or alternately a flow velocity peak, which is a result of the fact that the fanjet flow accelerates once more and forms a second shock wave in the downstream of the first one. The low pressure and high velocity zone stays nearly unchanged, which is different from the influence of the contraction ratio of the cowl afterbody. Figure 24b shows the

comparison of the skin friction coefficient of the core cowl and the plug. The skin friction coefficient in the upstream of the first shock wave decreases with the increasing fan nozzle exit angle. However, the skin friction coefficients in the downstream of the first shock wave increase. These changes are mainly caused by the fanjet flow velocity. There is one peak and two valleys for the skin friction coefficients in the downstream of the first shock wave in the model with the fan nozzle exit angle being equal to 10.5°. This is mainly caused by the flow separation, which resulted from the first shock wave-boundary layer interaction. The core cowl drag is affected by several aspects, i.e., Mach number before the first shock wave, the strength of the shock wave, the shock wave-boundary layer interaction, flow separation and the second shock wave for various fan nozzle exit angle. The location of the first shock wave and the projected area of the core cowl vertical to the engine axis are almost unchanged. These factors would lead to complex effects. Therefore, the trend of the core cowl drag is dependent on the combined effect of these factors with the increasing fan nozzle exit angle.

a)

b)
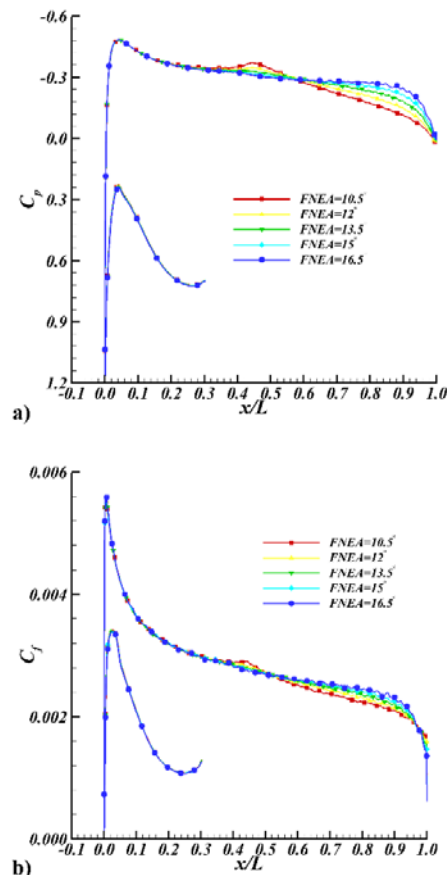
Fig. 22. Comparison of the distribution of a) the pressure coefficients, and b) the skin friction co-efficients on the surface of the cowl.

Figure 24 further shows that the difference of the

dimensionless static pressure and skin friction coefficients on the plug is so small that it can be neglected. That is why the pressure drag and the friction drag hardly change with the increase of the fan nozzle exit angle.

a)

b)

(c)
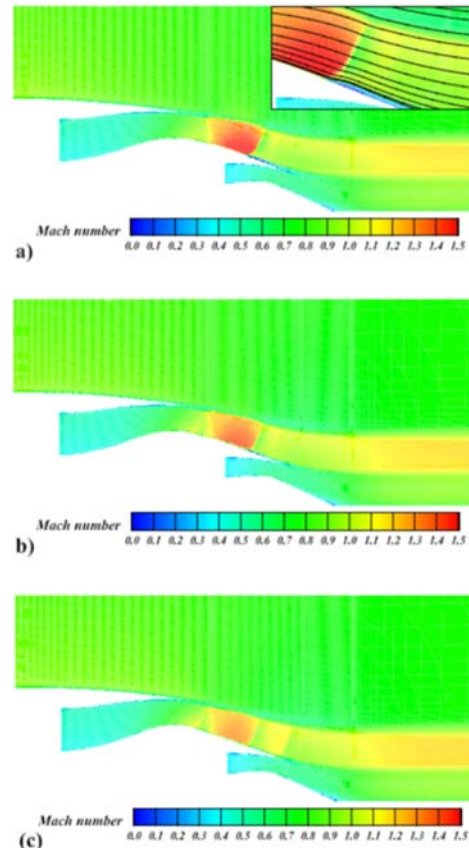
Fig. 23. Comparison of Mach number contour with varied fan nozzle exit angle: a) 10.5° , b) 13.5° , and c) 16.5° .

The fan nozzle thrust and the nacelle drag both drop upon the increase in the fan nozzle exit angle, and the reduction in the nacelle drag is more significant. As a result, the effective thrust continues to increase while the fan nozzle exit angle is increased.

1. CONCLUSIONS

In this paper, we studied the aerodynamic performance and flow characteristics of the nacelle and exhaust system. The influences of the geometric parameters (e.g., the contraction ratio of cowl afterbody and the fan nozzle exit angle) on their overall performance were investigated, and the related flow mechanism was explored. Our conclusions are as follows:

1. The flow field of the nacelle and exhaust system under the mid-cruise condition is of the characteristics of the transonic flow. A stagnation zone exits at the lip of the nacelle and there is a velocity peak on the forebody of

the nacelle. There are a number of complex flow phenomena in the downstream of the fan nozzle exit plane, such as the shockwave, the expansion wave, the shear flow, and the shock wave-boundary layer interaction. The magnitude of the fan nozzle thrust or the intake ram drag is much higher than that of the additional drag, the nacelle drag or the core nozzle thrust. And for the nacelle drag, the friction drag of the cowl (in the same order of magnitude as the pressure drag of the cowl, the core cowl and the plug) is much higher than the friction drag of the core cowl or the plug.
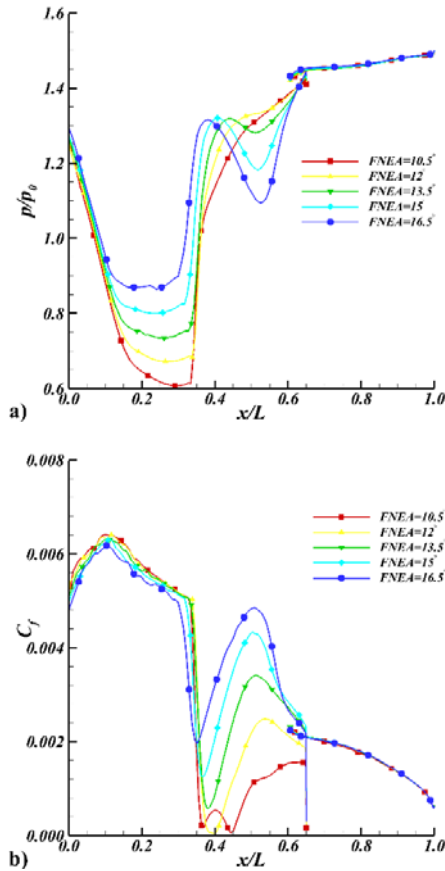
Fig. 24. Comparison of a) the dimensionless static pressure, and b) the skin friction coefficients distribution on the surface of the core cowl and the plug.

2. The effective thrust increases by 4.7% as the contraction ratio of the cowl afterbody increases and it increases by 2.4% as the fan nozzle exit angle increases. Regarding the influence of the contraction ratio of the cowl afterbody, the change of the nacelle drag is the dominant factor that affects the effective thrust. However, for the influence of the fan nozzle exit angle, the main affecting factors are the nacelle drag and the fan nozzle thrust. The pressure drag of the core cowl and the cowl are the main factors that affect the nacelle drag.

3. The degree of contraction ratio, the curvature and the projected area parallel and vertical to the engine axis of the core cowl are affected by the contraction ratio of the cowl afterbody. However, only the curvature of the core cowl is influenced by the fan nozzle exit angle. The design of the contraction ratio of the cowl afterbody and the fan nozzle exit angle can affect the issues including the Mach number before the first shock wave, the strength and location of the first shock wave, and the existence of the flow separation and second shock wave. These issues have influences on the pressure distribution on the core cowl and the surrounding flow velocity, and hence affect the core cowl drag.

4. The degree of the contraction ratio, the curvature and the projected area parallel and vertical to the engine axis of the cowl are affected by the contraction ratio of the cowl afterbody. However, only the curvature of the cowl is influenced by the fan nozzle exit angle. The factors mentioned above have influences on the distribution of the static pressure on the cowl afterbody and the surrounding flow velocity, and thus they further influence the cowl drag.

REFERENCES

Blumenthal, B. T., A. A. Elmiligui, K. A. Geiselhart, R. L. Campbell, M. D. Maughmer and S. Schmitz (2012). Computational investigation of a boundary-layer-ingestion propulsion system. *Journal of Aircraft* 134(6), 061016.

Christie, R., A. Heidebrecht and D. MacManus (2017). An automated approach to nacelle parameterization using intuitive class shape transformation curves. *Journal of Engineering for Gas Turbines and Power* 139(6), 062601.

Fang, X., Y. Zhang, S. Li and H. Chen (2016). Transonic nacelle aerodynamic optimization based on hybrid genetic algorithm. In *17th AIAA/ISSMO Multidisciplinary Analysis and Optimization Conferenc e AIAA 2016-3833*.

Gao, X., M. Li and Q. Li (2019). Study on intake drag characteristics of transport airplane with powered-on aeroengine in nacelle. *Journal of Propulsion Technology* 40(1), 61–63.

Gohardani, A. S., G. Doulgeris and R. Singh (2011). Challenges of future aircraft propulsion: A review of distributed propulsion technology and its potential application for the all electric commercial aircraft. *Progress in Aerospace Sciences* 47(5), 369–391.

Goulos, I., J. Otter, T. Stankowski, D. MacManus, N. Grech and C. Sheaf (2016 b). Aero- dynamic design of separate-jet exhausts for future civil aero-enginespart ii: Design space exploration, surrogate modeling, and optimization. *Journal of Engineering for Gas Turbines and Power* 138(8), 081202.

Goulos, I., T. Stankowski, J. Otter, D. Mac-Manus, N. Grech and C. Sheaf (2016a). Aerodynamic design of separate-jet exhausts for future civil aero-enginespart i: Parametric geometry definition and computational fluid dynamics approach. *Journal of Engineering for Gas Turbines and Power* 138(8), 081201.

Hei, S. H. (2016). *Numerical investigation on interaction between exhaust system and nacelle,* Master Thesis, Northwestern Polytechnical University, Xi'an, China.

Hirose, N., K. Asai, R. Kawamura and K. Ikawa (1991). Euler flow analysis of turbine powered simulator and fanjet engine. *Journal of Propulsion and Power* 7(6), 1015–1022.

Hoheisel, H. (1997). Aerodynamic aspects of engine-aircraft integration of transport aircraft. *Aerospace Science and Technology* 1(7), 475–487.

Isikveren, A. T., A. Seitz, J. Bijewitz, A. Mirzoyan, A. Isyanov, R. Grenon and S. Stckl (2015). Distributed propulsion and ultra-high by-pass rotor study at aircraft level. *The Aeronautical Journal* 119(1221), 1327–1376.

Joo, J., G. Tillman and R. Lin (2012). Nacelle external drag prediction using computational flu- id dynamics. In *In 48th AIAA/ASME/SAE/ASEE Joint Propulsion Conference and Exhibit* AIAA 2012-3998.

Lee, C. C. and C. Boedicker (1985). Subsonic diffuser design and performance for advanced fighter aircraft. In *Aircraft design systems and operations meeting* AIAA 1985-3073.

Li, S. Y. and Y. J. Zhong (2016). A turbofan-engine nacelle shape design and optimization method for natural laminar flow control. In *In ASME Turbo Expo 2016: Turbomachinery Technical Conference and Exposition. American Society of Mechanical Engineers Digital Collection* ASME GT2016-57463.

Lin, A. Q., J. Zhou, X. J. Tian and H. Zhang (2019). Effective boundary conditions and numerical method for flow characteristics of aero-engine compressor at high mach flight. *Journal of Applied Fluid Mechanics* 12(3), 845–855.

Peyvan, A. and A. H. Benisi (2016). Axial-flow compressor performance prediction in design and off-design conditions through 1-d and 3-d modeling and experimental study. *Journal of Applied Fluid Mechanics* 9(5), 2149–2160.

Qiang, X. (2013). *Integrated design of civil engine nacelle and exhaust system.* Master Thesis, Northwestern Polytechnical University, Xi'an, China.

Robinson, M. H., K. R. D. G. MacManus and C. Sheaf (2017). Short and slim nacelle design for ultra-high bpr engines. In *55th AIAA Aerospace Sciences Meeting* AIAA 2017-0707.

Savelyev, A., N. Zlenko and S. Mikhaylov (2014). Shape optimization of the engine nacelle using rans. In *International Conference on the Methods of Aerophysical Research* https://www.researchgate.net/profile/Andrey_ Savelyev/publication/323390827_Shape_Opti mization_of_the_Engine_Nacelle_Using_RA NS/links/5a931acd0f7e9ba4296f4a76/Shape-Optimization-of-the-Engine-Nacelle-Using-RANS.pdf. 2020-07-30.

Schnell, R., J. Yin, C. Voss and E. Nicke (2012). Assessment and optimization of the aerodynamic and acoustic characteristics of a counter rotating open rotor. *Journal of Turbomachinery* 55(3), 1141–1153.

Singh, R., P. L. V. Pachidis and P. Pilidis (2014). Opportunities and challenges for distributed propulsion and boundary layer ingestion. *Aircraft Engineering and Aerospace Technology: An International Journal* 47(5), 369– 391.

Wang, W. J., Z. X. Wang, L. Zhou and J. W. Shi (2019). A numerical simulation on the coupled influence of the high bypass raito turbofan nacelle and exhaust system. *Journal of Engineering Thermophysics* 40(9), 1981–1987.

Xiong, J., X. Y. Wang, Y. Q. Shi, and Z. G. Yan (2012). Aerodynamic optimization design of high bypass ratio separate-flow exhaust system based on parallel multi-objective genetic algorithm. *Journal of Aerospace Power* 27(6), 1384–1390.

Yangaz, M. U., G. A. iftiolu and A. N. Kadrgan (2016). Comparison of conventional and modified burners in performance with different fuels using a linear and a non-linear eddy-viscosity turbulence model. *Journal of Applied Fluid Mechanics* 12(6), 2069–2081.

Zhong, Y. J. and S. Y. Li (2017). A 3d shape design and optimization method for natural laminar flow nacelle. In *In ASME Turbo Expo 2017: Turbomachinery Technical Conference and Exposition.* American Society of Mechanical Engineers Digital Collection.